Supplementary Information

Record stack durability in industrial solid oxide steam electrolysis through operational control

Authors: Vasileios Bilalis[1,2],Olivia Fjord Sloth[1,2], Thomas Erik Lyck Smitshuysen[2], Javid Beyrami[1], Marie Lund Traulsen[2], Martin Nørby Nielsen[2], Dario Montinaro[3], Jan Pieter Ouweltjes[4], Henrik Lund Frandsen[1], Ming Chen[1], Mogens Bjerg Mogensen[1], Søren Højgaard Jensen[2,5*], Vincenzo Esposito[1*]

Affiliations:

[1]DTU Energy, Technical University of Denmark, Fysikvej Building 310, 2800 Kgs. Lyngby, DK
[2]DynElectro ApS. Syvvejen 10, 4130 Viby Sjælland, DK
[3]SolydEra SpA. Viale Trento 115/117, 38017 Mezzolombardo, IT
[4]SolydEra SA. Avenue des Sports 26, 1004 Yverdon-les-Bains, CH
[5]Aalborg University, Department of Energy. Pontoppidanstræde 111, 9220 Aalborg, DK

*Corresponding authors Emails: vies@dtu.dk, soren@dynelectro.dk

Table of Contents

Supplementary Note 1. World-Record Durability for a Full SOEC Stack and Benchmark Experiment for the Green H_2 Industry

There are three main types of electrolysis cells: alkaline electrolysis cells (AECs), proton exchange membrane electrolysis cells (PEMECs), and solid oxide electrolysis cells (SOECs). AECs first developed by Troostwijk and Deiman in 1790 and reached industrial scale in 1939[1]. AECs remain cost-effective, with investment costs of USD 500–1000/kW and lifetimes up to 90000 h. However, suffer from low current densities (0.1–0.5 $A \cdot cm^{-2}$), reliance on corrosive KOH electrolytes and the associated risk of forming flammable gas mixtures[2–4]. PEMECs developed by Grubbs and General Electric in 1966 usually operate at 30–80 °C, under higher current densities (1–2 $A \cdot cm^{-2}$) than AECs, and produce ultra-pure H_2 and oxygen (O_2)[5]. Modern PEMEC systems can operate for approximately 60000 h[2,3]. However, they require high-purity inlet gases, cannot operate with hydrocarbons, and have high CAPEX cost driven by the extensive use of noble metals (e,g, Ir, Pt) in the cell and the cost of bipolar plates[3,6]. AEC systems exhibit degradation rates of 0.25–1.5% per year[7,8]. In comparison, PEMEC systems, while offering similar operational lifetimes, typically experience slightly higher degradation of 0.5–2.5% per year[9,10].

SOECs were first developed in the 1970s by General Electric and Brookhaven National Laboratory, with later advancements by Dornier in Germany[8]. Advantages include reversible operation (switching between SOEC/SOFC), fuel flexibility, and straightforward integration with chemical synthesis processes such as methanol and ammonia production[11–13]. Commercial deployment, however, is hindered by limited durability, with full SOEC stacks using yttria-stabilized zirconia (YSZ) electrolytes exhibiting lifetimes below 10,000 h[14,15].

Recent development efforts on SOC have focused on mitigating degradation; however, long-term durability remains a critical challenge for large-scale deployment. Notably, in SOFC mode, the longest durability test reported to date is that of a two-cell stack operated at 700 °C for up to 100,000 h, with 93,000 h sustained at a current density of +0.5 $A \cdot cm^{-2}$ [16,17]. The tested stack exhibited a stable voltage degradation rate of approximately 0.5% kh^{-1}. This level of durability, both in lifespan and performance, has not yet been achieved in SOEC systems, highlighting the importance of polarization direction in SOC degradation. Hua et al. presented a comprehensive review of SOEC durability tests, consolidating, among others, key findings from long-term tests at the cell, short-stack, and full-stack levels[18]. **Table S1** summarizes, in order of decreasing operational duration, the longest durability tests conducted with SOEC stacks. The table includes only tests performed at electrolysis current densities≥ -0.5 $A \cdot cm^{-2}$

and lasting more than 3000 h. It appears that reports documenting low degradation rates beyond 20000 h are still a few. Among durability studies that meet both the current-density and duration criteria, the lowest reported voltage degradation rates are approximately 4 $mV \cdot kh^{-1}$ and 0.5% kh^{-1}. By comparison, the degradation rate of 0.05% kh^{-1} achieved in our study and determined over 22,000 h of stack operation, is one order of magnitude lower than the lowest previously reported value.

Table S1. Comparative summary of SOEC stacks durability tests (t>3000 h and i ≥ −0.5 A·cm⁻²).

Company / Organization	No. of Cells	Cell area (cm^2)	*T* (°C)	*I* (A cm^{-2})	*T* (h)	*D.R. (voltage)* (% per kh)	Ref. (year)
Solydera (Dynelectro)	70	80	750	-0.5	25,000	0.23 =>0.05 (& 1.4 $m\Omega \cdot cm^2\ kh^{-1}$)	This study, (2026)
Jülich (F1002-165)	2	80	700– 800	−0.5	23,000	0.4–1.9	[19,20] (2018)
Jülich (Forschungszentrum)	—	80	800	−0.5	21,363	0.7	[19,20] (2018)
Jülich (F10 design)	2	80	800	−0.5	18,000	0.6	[20] (2018)
SolidPower (EIFER)	6	48	710 – 730	−0.6 ~ −0.5	10,700	0.54	[21] (2017)
Sunfire (CEA)	30	128	830 - 850	-0.52	9,500	12 $m\Omega \cdot cm^2\ kh^{-1}$	[15] (2024)
Sunfire Gmbh (EIFER)	5	128	847	−0.9	6,000	2	[18] (2016)
Topsoe Fuel Cell (EIFER)	25	87.7	772	−0.72	5,640	3.2	[22] (2015)
Sunfire Gmbh (CEA-LITEN)	30	—	830–840	−0.65	5,500	0.8	[18] (2022)
Fraunhofer IKTS	30	127	800	−0.40	5,000	0.6	[23] (2017)
Sunfire Gmbh (CEA-LITEN)	30	—	830–860	−0.65	4,500	0.7	[18] (2022)
Topsoe Fuel Cell (DTU)	—	701.6 (total)	800	−1.0	4,300	2.64	[18,24] (2013)
Sunfire Gmbh (EIFER)	30	128	830	−0.5	4,224	0.8	[25] (2021)
Sunfire MK225 (DLR)	30	128	820	−0.52	3,750	0.5	[26] (2020)
Ceres	10	—	600	−0.40	3,500	20 $m\Omega \cdot cm^2\ kh^{-1}$	[27] (2023)

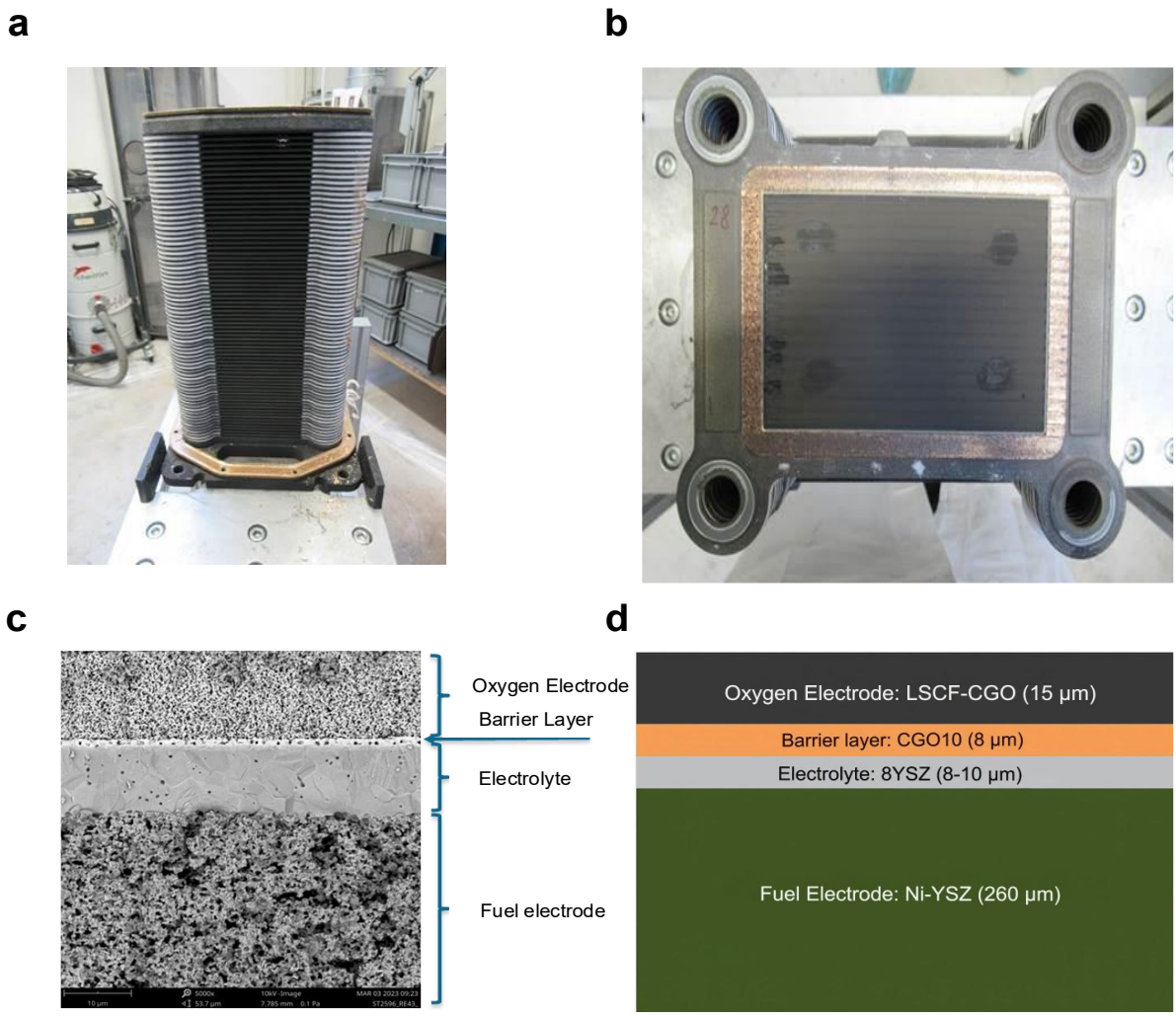

Fig. S1. Stack design and architecture of the single SOEC. a, Photograph of the assembled planar stack with metallic interconnects and compression hardware; **b,** Top view of a single repeating unit showing the sealing frame and flow field/rib structure; the dark central region corresponds to the electrochemically active area. **c,** Cross-sectional SEM of one cell highlighting, from top to bottom, the LSCF–GCO oxygen electrode, a thin GGO10 barrier layer, a dense 8YSZ electrolyte (8–10 µm), and the Ni–YSZ FE (~260 µm). **d,** Schematic of the layer sequence used in this study.

Supplementary Note 2. Safety control, testing parameters and AC:DC operating protocol

The test bench was installed with safety features. In its safety mode, electrolysis current is interrupted by an interlock, and valves to gases are forced closed, except for air and safety gas 5% H_2 in N_2. The safety mode is triggered by stack temperature < 580°C, LEL sensors indicating increased levels of explosive gases, ventilation < 13 m^3 min^{-1}, and flow of cooling water to prevent water condensation on the fuel outlet. Additionally, the power supply was limited to -60 A at 49-105 V, which violates the electrolysis power requirements. A lower limit of hydrogen flow was specified to 0.3 NL min^{-1}, triggering a flow of 10 NL min^{-1} safety gas on the FE. In case of hard power failures or similar, the test bench is hardware-fixed on a safety flow of 10 NL min^{-1} of safety gas, and air on the FE and OE, and the resulting cooling is ~1 °C min^{-1} until 180°C is reached, and OE-outlet and gas-flow stops, if power is on. In failures where an operator was present, the procedure was to stabilize the stack temperature in safety flow, then gradually increase airflow to 200 NL min^{-1} and heat the stack to operating temperature at 1 °C min^{-1}.

The stack was operated in AC:DC electrolysis mode at an average current density of – 0.5 A cm^{-2} and an inlet temperature of 750 °C. The Ni-YSZ FE was supplied with 31.1 NL min^{-1} of steam (evaporated with an Adrop using MilliQ-water) and 3.5 NL min^{-1} of H_2, provided either from storage or by recycling the produced H_2 gas to maintain the desired H_2 concentration. This corresponded to 10% H_2 in the inlet gas and a steam conversion of 63%. The resistivity of the Milli-Q water decreased from approximately 15 MΩ·cm at the purification unit to around 4 MΩ·cm downstream at the evaporator, indicating a deterioration in water quality within the balance-of-plant. Previous studies have shown that even purified water with resistivities around 10 MΩ·cm may still contain harmful trace impurities, particularly Si- and B-containing species, which are only weakly retained by ion-exchange systems. Such impurities can be transferred into the steam phase and contribute to SOEC degradation.

The LSCF-CGO Oxygen Electrode (OE) was fed with 372 NL min^{-1} of dried and filtered air (dew-point at -40 °C, downstream high-surface carbon filter). After 2060 h of operation, the H_2 concentration in the FE feed was reduced to 2% by lowering the H_2 flow to 0.7 NL min^{-1}. After 4300 h, the air flow was decreased to 200 NL min^{-1}.

The stack was operated inside an insulated hotbox, not inside a furnace, and there was no active heating of the hotbox during operation beyond the heat generated by the stack itself under AC:DC operation. In particular, the stack was not gas-heated, and no additional electrical heat tracing was applied to the hotbox. The inlet gases were preheated to 750 °C using external heat tracing before entering the stack. Under these conditions, the reported stack temperature reflects the thermal state of the stack/hotbox assembly. The temperature drop observed during EIS measurements at OCV is attributed to the absence of active hotbox heating under open-circuit conditions; it therefore primarily reflects heat loss from the hotbox when the stack is no longer generating sufficient internal heat. The thermocouples were positioned in-line in the gas paths, directly at the interfaces between the gas manifolds and the stack. Temperatures were thus recorded at both the fuel-electrode (FE) and (OE) inlets and outlets. The temperature

sensors are K-type thermocouples placed in the gas path, right below the interface between the gas manifold and the stack. The pressure transducers are placed outside the stack, with tubing leading into the manifold to measure the gas path. The pressure drop across the stack was 6 to 8 mbar on the OE and 5 to 3 mbar on the FE, depending on the atmospheric pressure and temperature found downstream of the gas outlets

The reported nominal temperature difference across the stack was calculated as:

$$\Delta T_{nom} = \frac{(T_{FE,out} + T_{OE,out}) - (T_{FE,in} + T_{OE,in})}{2}$$

This quantity therefore represents the average gas temperature increase across the stack, based on the measured inlet and outlet temperatures on both the FE and OE sides.

AC:DC operation was primarily conducted at 30 Hz, with each AC:DC cycle lasting 33 ms. This choice is consistent with earlier AC:DC SOEC work[28] , and is also supported by later study[29]. The current in electrolysis mode was - 48.3 A, and in fuel cell mode, 46.3 A, for an average current of 40.35 A. The cells had an active electrode area of 80 cm^2, giving a current density of - 0.5 A cm^{-2}. The transition time between electrolysis and fuel cell mode was less than a millisecond, ensuring optimal AC:DC operation without compromising the power supply limitations. A bidirectional power supply (Regatron G5.RSS) was used to generate the AC:DC current. For detailed monitoring, the stack was fitted with wiring that enabled voltage measurements at the cluster level.

Supplementary Note 3. Long-term performance benchmarking. Degradation-rate extraction methodology

Table S2 summarises the degradation indicators by tracking the stack-voltage evolution over six labelled periods (Period 3 split into two sub-periods). The table reports the initial and final voltages (V_{in}, V_{fin}), the time window ($\Delta t = t_{fin} - t_{in}$), and voltage-degradation rates in V per 1,000 h ($V \cdot kh^{-1}$) and ΔV% per 1,000 h (% kh^{-1}). Briefly, the early, short periods show the largest changes, whereas the longer period at 750 °C shows very low average rates, consistent with stable long-term operation. This note details how stack-level degradation rates are computed and reported for each operating period, using only the quantities listed in the period table.

Absolute rate ($V \cdot h^{-1}$ and $V \cdot kh^{-1}$): The absolute drift rate in volts per hour is:

- $\Delta V/\Delta t = (V_{fin} - V_{in})/ (t_{fin} - t_{in})$, in $V \cdot h^{-1}$ (1)

For reporting in V per 1000 hours ($V \cdot kh^{-1}$), we rescale by 1000:

- $Dr = \Delta V/\Delta t$ *1,000, in $V \cdot kh^{-1}$ (2)

Relative rate (% kh^{-1}): To express the change relative to the period's initial stack voltage, we divide the absolute rate (in V per kh) by V_{in} and convert to percent:

- $DR = ((V_{fin}-V_{in})/V_{in})/(t_{fin}-t_{in}) * 1000 * 100$ (3)

This yields the percentage voltage change per 1000 h referenced to the start of the window.

Degradation periods. The dataset is separated into two periods: an initial period with multiple operation modes and conditions, followed by a single long AC:DC period at 750 °C. For the three aggregated periods, degradation rates are computed from the overall endpoints of the aggregated window. The same formulas as above are then applied to obtain V h^{-1}, V kh^{-1}, and %/kh^{-1}.

Table S2. Summary of the different operating periods and conditions of the durability test.

Period	**Mode (°C)**	***I*** **(A cm^{-2})**	t_{in} **(h)**	t_{fin} **(h)**	**Δ*t*** **(h)**	V_{in} **(V)**	V_{fin} **(V)**	***Dr*** **(V kh^{-1})**	***DR*** **(% kh^{-1})**
1st	DC (730°C)	0.50	70	208	138	81.4	82.7	9.4	11.5
2nd	ACDC (750°C)	0.50	252	392	140	80.2	80.3	0.7	0.9
3rd (a)	ACDC (700°C)	0.50	475	544	69	91.1	91.5	5.8	6.4
3rd (b)	ACDC (700°C)	0.20	621	751	130	73.3	73.9	4.6	6.3
4th	ACDC (750°C)	0.50	780	2060	1280	85.4	86.1	0.5	0.6
5th	DC (750°C)	0.50	2119	2715	596	91.2	91.1	0	0
6th	ACDC (750°C)	0.50	2813	25081	22268	85.2	86.2	0.04	0.05

Degradation Period	t_{in} **(h)**	t_{fin} **(h)**	***Δt*** **(h)**	V_{in} **(V)**	V_{fin} **(V)**	***Dr*** **(V kh^{-1})**	***DR*** **(% kh^{-1})**
1st	70	2715	2645	81.4	91.1	3.68	4.52
2nd	2813	25081	22268	85.2	86.2	0.04	0.05
Overall	70	25081	25011	81.4	86.2	0.19	0.23

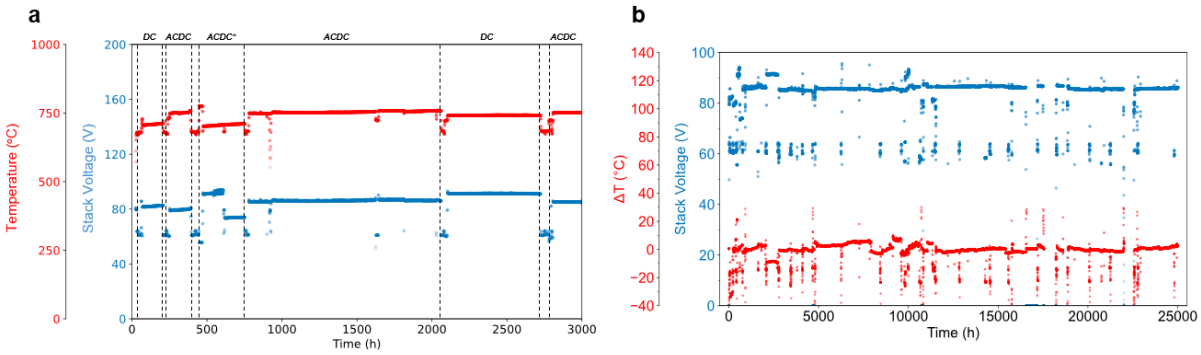

Fig. S2. Long-term electrochemical performance of the stack. a, Evolution of the stack's voltage and imposed average stack's temperature during the first 3000 h of operation (1st period). The different operation periods are marked on the plot; **b,** Evolution of the stack's voltage, and temperature difference between the gas inlet and outlet of the stack (ΔT), for the entire operation period. Intermittent white periods are EIS measurements. ΔT was calculated as $\Delta T = [FE_{in}+OE_{in}-(FE_{out}+OE_{out})]/2)$.

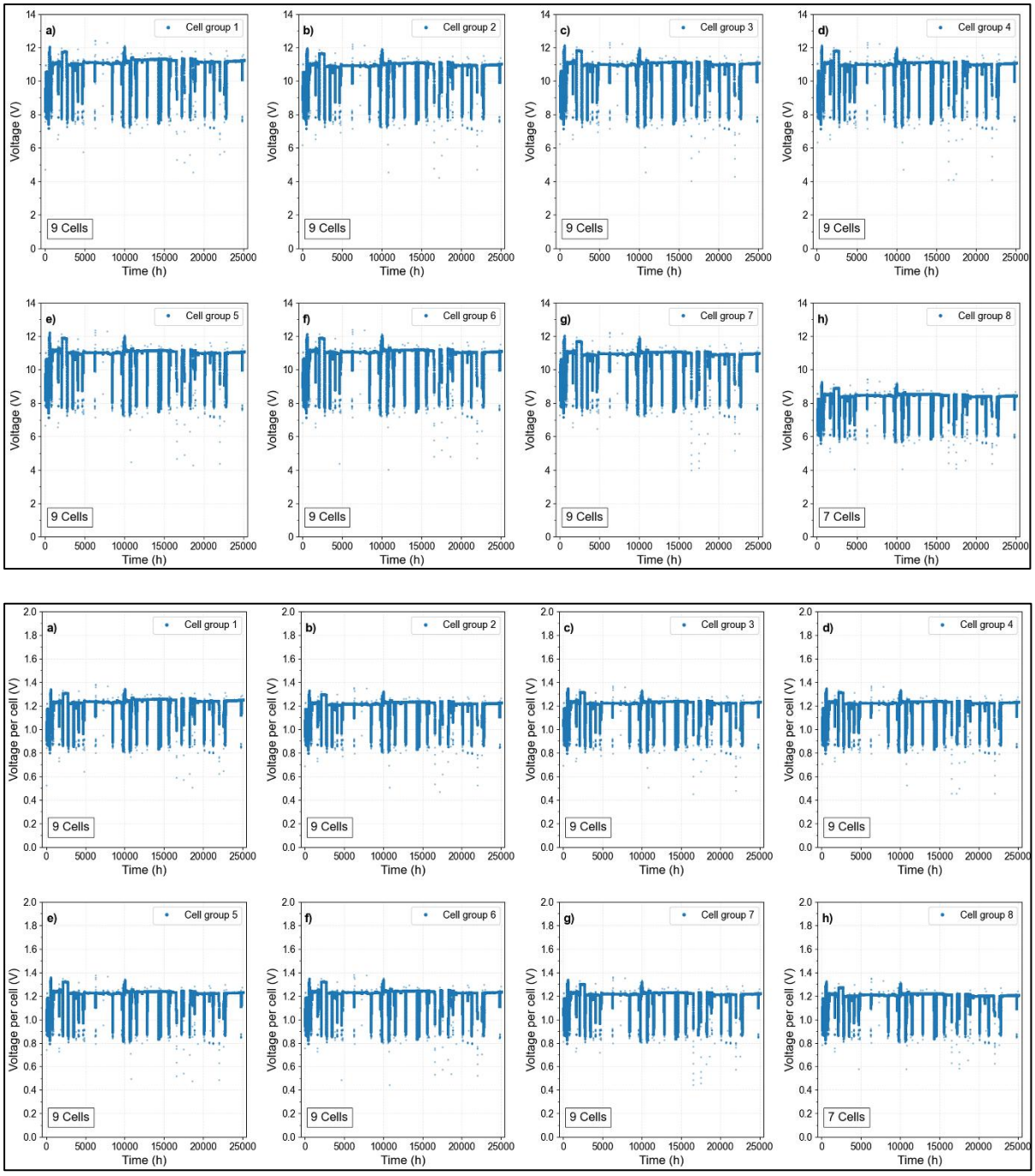

Fig. S3. Evolution of cell-group voltages over the 25,000 h operating period. Top panel (a–h): Average voltage of each cell group as a function of time. Cell groups 1–7 each comprise nine SOECs, while cell group 8 comprises seven SOECs. **Bottom panel (a–h):** Corresponding average voltage normalized by the number of cells in each group (voltage per cell). The close overlap of both the group voltages and the normalized cell voltages demonstrates the highly uniform electrochemical performance and degradation behavior across the stack, indicating homogeneous operating conditions and current distribution among the different cell groups.

Supplementary Note 4. Electrochemical impedance spectroscopy methodology

EIS measurements were conducted using a PicoScope (PicoTech 5000D) in conjunction with a current sensor (DaniSense DS200UB-10V). High-resolution voltage and current signals were acquired and subsequently processed with a custom-built frequency analyser. The EIS were recorded with 12 measurement points per decade from 0.09 Hz to 200 kHz, and with a perturbation amplitude of 12.5 mA cm^{-2} (galvanostatic AC perturbation). All EIS measurements were performed at OCV under four distinct measurement conditions at 700 °C. The 700 °C temperature was selected for the EIS OCV data because the air preheater and heat ropes are considered at risk of damage at 750 °C. The distinction between mass-transport–limited phenomena and thermally activated processes at the FE and the OE was thereby facilitated. The gas compositions and flows corresponding to each measurement scenario are summarized in **Table S3.** The EIS data presented and analysed in this paper correspond to Condition A.

Table S3. Gas compositions and volumetric flows used during EIS measurements, conducted at 700°C.

Measurement Conditions	**Fuel Electrode (FE)**		**Oxygen Electrode (OE)**	
	Inlet Fuel Gas composition	Total flow (NLPM)	Inlet Oxygen content	Total flow (NLPM)
Condition A	8% H_2 / 92% H_2O	37	21%	372
Condition B	17% H_2 / 83% H_2O	35	21%	372
Condition C	17% H_2 / 83% H_2O	35	12%	175
Condition D	17% H_2 / 83% H_2O	35	21%	200

Supplementary Note 5. Distribution of relaxation times (DRT) analysis and EIS fitting on Equivalent Circuit Model (ECM)

The DRT analysis was conducted using the open-source Python toolbox *dearEIS*[30]. The parameterrs used in the DRT algorithm are listed in Table S4.

Table S4. Fitting parameters used in the DRT analysis using *dearEIS* tool.

Parameter	Value
Method	TR–RBF
Discretization method	Gaussian
Data used	Combined Re Im
Derivative order	1st
Regularization parameter	1×10^{-4}
Shape Type	FWHM
Induction	Not included
Shape coefficient	0.5

The DRT analysis of the EIS data recorded under the four different measurement conditions (Fig. S4a) and during the durability test (Fig. S4b), revealed five distinct polarization processes. Based on these findings, a suitable equivalent circuit model (ECM) was used for the complex nonlinear square (CNLS) fitting of the EIS data. The ECM was composed of seven lumped electrical elements connected in series: One inductor (L), one resistor (Rs), and five *RQ* elements. The inductor corresponds to the high-frequency region of the recorded EIS and is used to model the inductive behaviour that produces impedance "tails" curving inward and/or outward. This phenomenon was predominantly observed in groups G5 and G8 and is attributed to the electrical wiring and components associated with these groups, rather than to the electrochemical performance of the stack itself (Fig. S5).

The *Rs* element accounts for the ohmic resistance of the tested system, while the five *RQ* elements represent the polarisation processes. These *RQ* elements are indexed in decreasing frequency order (i.e., RQ_1 = highest frequency, … , RQ_5 = lowest frequency). To successfully fit the 640 (8 group cell*20 EIS*4 conditions) EIS recorded during testing, it was decided to keep fixed the n parameters of the respective RQ elements at defined values. The corresponding n values for the respective RQ elements are: $n_1 = 0.94$, $n_2 = 0.93$, $n_3 = 0.76$, $n_4 = 1.0$, and $n_5 = 1.0$.

In this study, only the extracted resistances related to Condition A are presented. For the CNLS fitting process, an initial parameter guess was provided and subsequently optimised to match the data. This guess was guided by the findings of the DRT analysis (resistance and frequency values). To efficiently process the large number of spectra, a Python script was developed to automate the interaction with *dearEIS* and streamline the analysis workflow.

To achieve reliable fits with small residual error, it was essential to provide a good initial guess. Since the EIS data showed minimal variation after approximately 2080 h, the same initial guess could be reused for Groups 1, 2, 3, 4, 6, and 7 (batch fitting). However, Group 5 often required manual adjustment of the initial guess due to its distinct inductive characteristics, and in some cases, Group 8 also required it.

In addition, constraints had to be applied to some of the initial guesses to ensure proper element separation. Without such limitations, the process frequencies represented by the RQ_2 and RQ_3 elements occasionally overlapped during fitting, reducing both the clarity and the reliability of the model.

Regarding the CNLS fitting algorithm, the weight function applied was modulus $1/|Z|$. No restrictions were imposed on either the maximum number of function evaluations or the time allowed for convergence.

Following the same approach used for voltage, the degradation rates of *RS* and *R2* were calculated over the aggregated operation periods (Table S5). For each resistance component, the start and end values of the corresponding period, together with its duration, were used to determine the absolute ($\Omega \cdot cm^2 \cdot kh^{-1}$) and normalized ($\% \cdot kh^{-1}$) degradation rates.

For *Rtot* degradation rates, all *Rtot* values obtained from the EIS measurements recorded within each of the two operation periods were considered. The degradation rates between consecutive measurements were first calculated and then averaged to obtain a representative degradation rate for each of the two operation periods. As shown in Table S5, the standard deviation of these average rate values is very low, indicating good consistency in the calculated degradation rates.

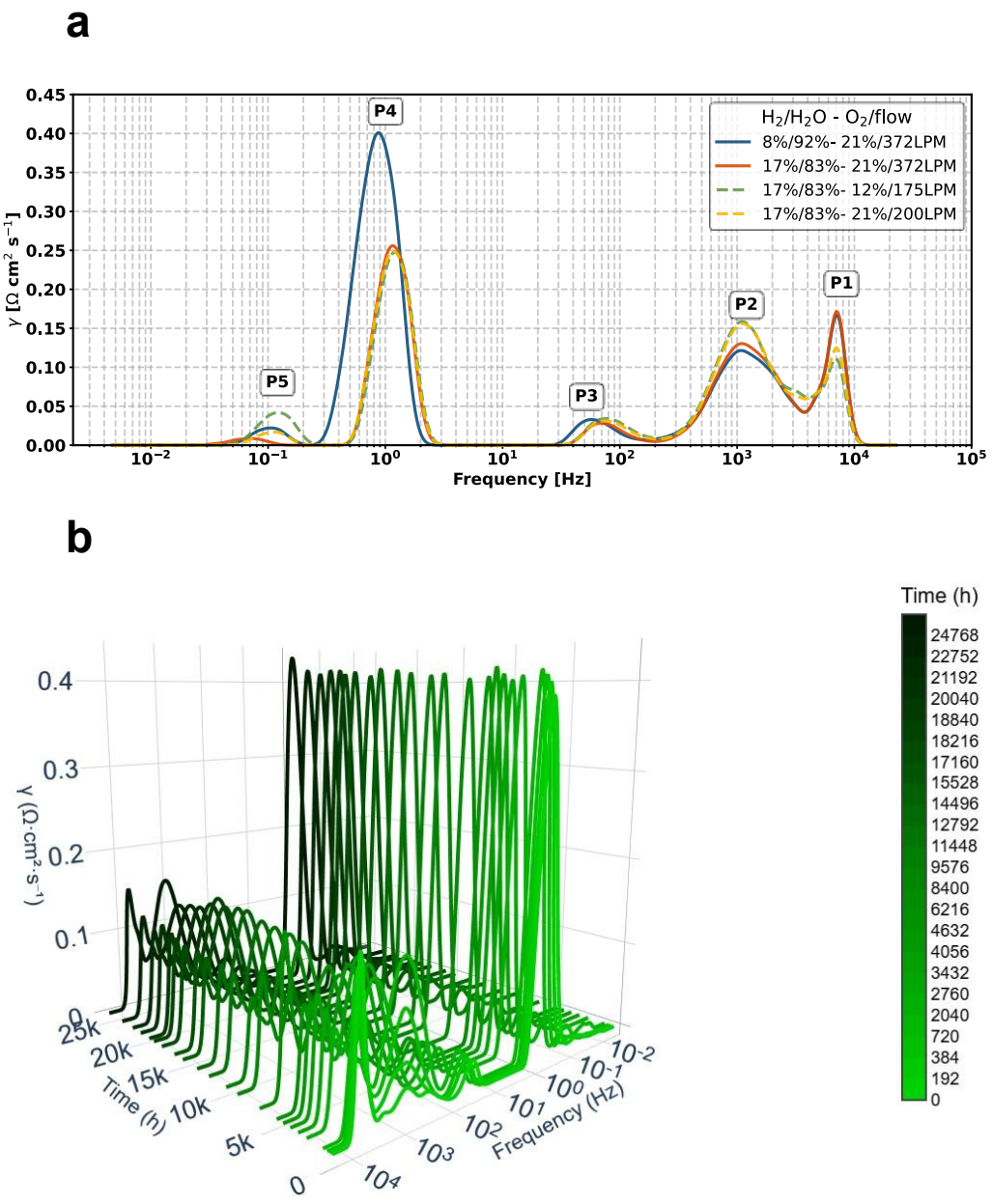

Fig. S4. DRT plots of a cell group under varied $H_2/H_2O–O_2$ flows and during long-term testing. **a,** Representative example of the DRT plots of EIS data recorded under the four different measurement conditions (legend). The distinct relaxation processes are labelled P2–P5. **b,** Waterfall (3D) representation of DRT evolution under Condition A, encoded by colour (green→black), showing the evolution of the DRT features during operation.

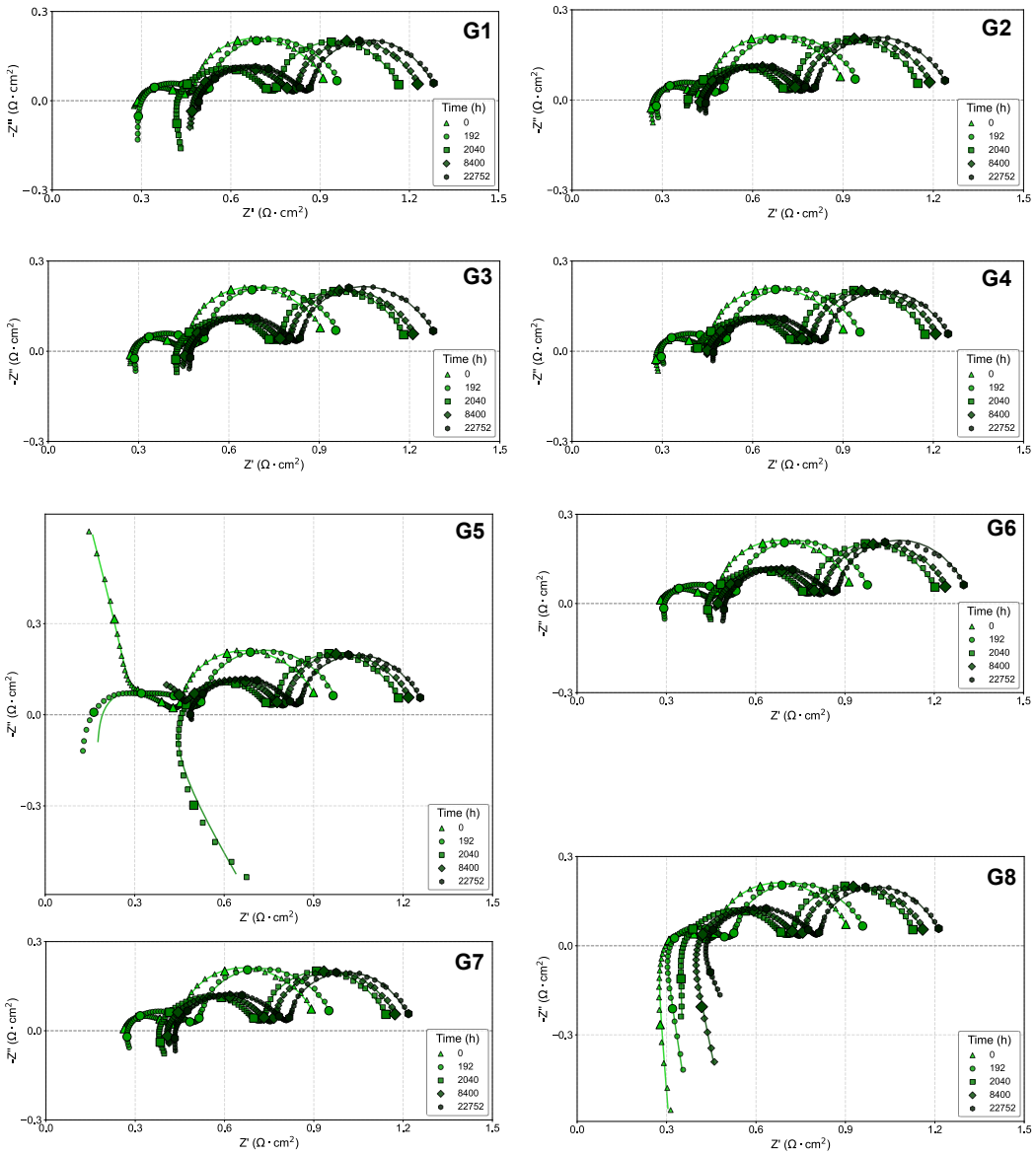

Fig. S5. ECM-fitted Nyquist plots of EIS recorded for the eight cell groups of the stack during operation. G1–G8 are the IDs of the eight different cell groups. Symbols denote measured EIS at selected five-time intervals (legend), with colour encoding time from green (start of test) to black (end of test). Solid lines are the fits obtained with the equivalent-circuit model (ECM) described in the Methods; the same model and fitting constraints were applied to all groups. The displayed EIS data were recorded under Condition A. The high-frequency inductive tails observed in G5 and G8 are typical EIS artifacts related to the electrical wires and connections of these cell groups, not to their electrochemical performance.

Table S5. Resistance degradation rates of the different degradation periods

Degradation parameter	Initial degradation period (0 h –2700 h)	Final degradation period (2760 h – 25000 h)	Overall degradation period (0 h –25000 h)
$\Delta Rtot/dt$ (Ω cm^2 kh^{-1})	0.23 (std=0.18)	0.001 (std=0.016)	0.06 (std=0.13)
$\Delta Rs/\Delta t$ ($\Omega \cdot cm^2 \cdot kh^{-1}$)	0.5	0.003	0.009
$\Delta R2/\Delta t$ ($\Omega \cdot cm^2 \cdot kh^{-1}$)	0.57	0	0.006
$\Delta Rtot$ (% kh^{-1})	0.22 (std=0.18)	0.001 (std=0.013)	0.06 (std=0.13)
ΔRs (% kh^{-1})	1.92	0.08	0.2
$\Delta R2$ (% kh^{-1})	5.35	0	0.26

Supplementary Note 6. Post-mortem microstructural characterization

Scanning Electron Microscopy (SEM): Microstructural characterization was performed using a Zeiss Merlin thermal field emission-SEM (FEG-SEM) equipped with an Angle -selective Backscattered (AsB) detector. This configuration enables high contrast discrimination of the pore phase within the Ni–YSZ matrix of the FE. AsB images were therefore used to detect porosity changes and interfacial damage of the matrix of the Ni-YSZ FE. AsB images at different magnifications and locations were acquired in both the inlet and outlet regions. To resolve spatial variations in microstructure near the FE/electrolyte interface, special focus was placed on the regions 5 to 10 μm from that interface. Both high- and low-magnification AsB images were obtained at an accelerating voltage of 15 kV and a working distance of 3.9–4 mm.

Prior to imaging, the epoxy-embedded specimens were carbon-coated to minimize charging, and carbon tape was used to ensure reliable electrical contact with the sample holder.

To observe changes in the matrix of the percolated Ni (brightest contrast), complementary low-voltage (1 kV) images were obtained using the Inlens detector at a 4 mm working distance and different magnifications. This established imaging approach provides robust differentiation of electrically connected Ni from the ceramic components[31]. The epoxy samples used for this

imaging were not carbon-coated, but only carbon tape was applied around the embedded specimens.

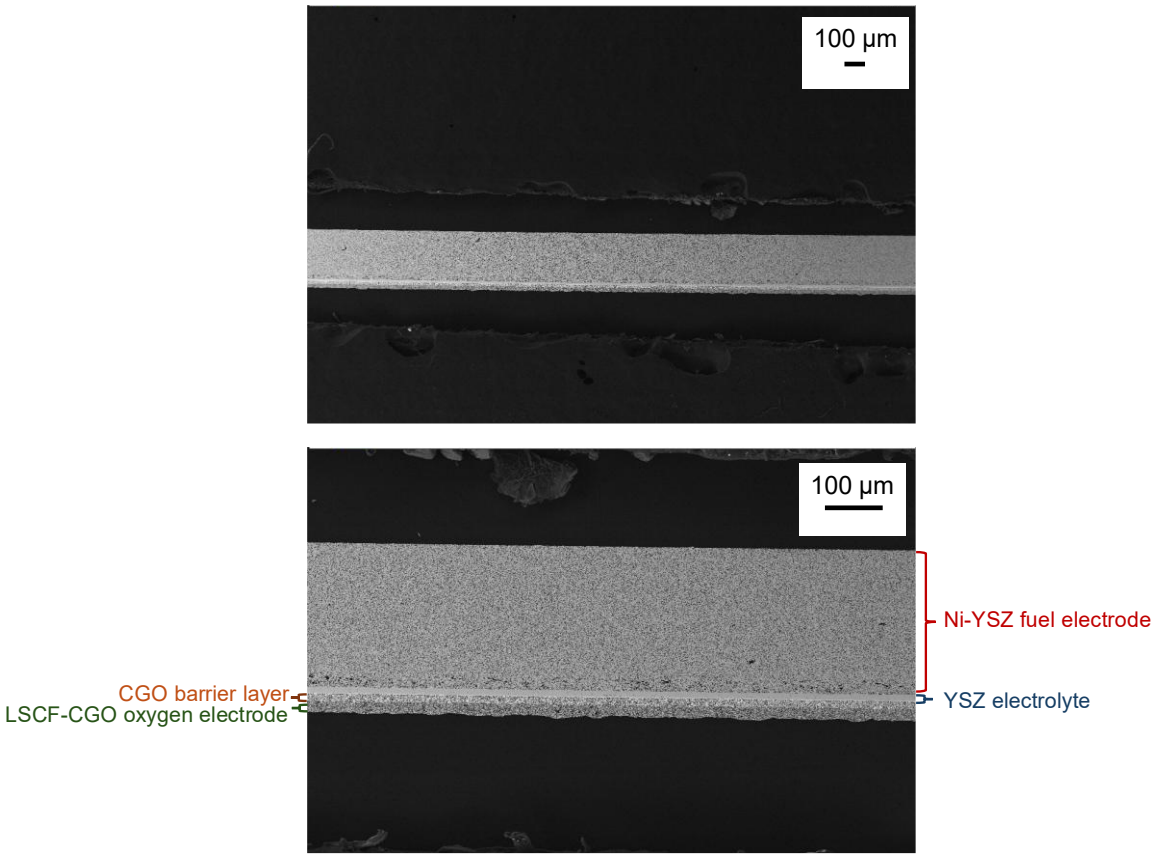

Fig. S6. Investigated cross-sectional AsB-SEM image of the single SOC layered architecture. Two fields of view with different magnification. AsB contrast highlights the compositional layering, showing the Ni–YSZ fuel electrode, YSZ electrolyte, CGO barrier layer, and LSCF–CGO oxygen electrode (as annotated). Dark regions correspond to the epoxy embedding medium.

Supplementary Note 7. Quantification of area pore-fraction using AsB-SEM images.

Area pore fraction (2D porosity) was quantified from the AsB images using ImageJ[32]. The images were exported in an 8bit grayscale format and imported directly into ImageJ. Prior to analysis, each image was cropped to exclude external borders, scale bars, and nonrepresentative areas of the microstructure. To isolate the pore phase, we employed intensity-based segmentation. The threshold range was then adjusted so that values from 0 to the automated Otsu threshold (typically ~128 for binary images) were included. This selection highlights the pore regions in red in the threshold preview exclusively. With the threshold active and the above options enabled, ImageJ returns the pore fraction as %Area, corresponding to the ratio:

$$\text{Area pore fraction} = \frac{A_{\text{pores}}}{A_{\text{total}}} \times 100\% \quad (4)$$

To probe a broader portion of the Ni-YSZ electrode/electrolyte interface and minimize field-of-view bias, SEM images were acquired at multiple magnifications. In all cases, the Ni–YSZ matrix after testing is overall less porous (i.e., exhibits a smaller area pore fraction ΩΑΛΘΕ) than the untested reference, which is a typical signature of Ni coarsening. In the regions adjacent to the electrolyte, the microstructure in the 25,000 h tested cell appears locally slightly more porous in Figs. S7 and 8c–8d than in the untested sample. However, this measured pore fraction can be attributed to a few large pores randomly distributed along the interface. At higher magnification, this random distribution is less pronounced, and the pore fraction becomes smaller in the tested sample (Figs. S8a–b). In any case, the small difference in the porosity values between the two samples indicates substantial suppression of Ni migration, which would otherwise have caused a significant increase in porosity near the electrolyte region of the tested sample.

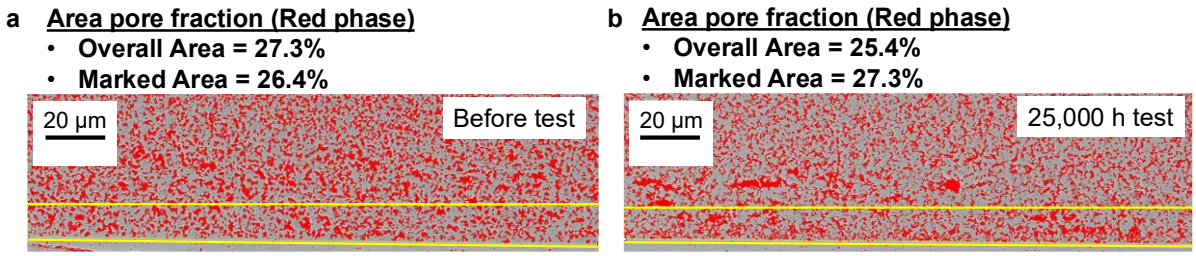

Fig. S7. Area pore-fraction analysis based on AsB-SEM images at the inlet of the Ni-YSZ FE before and after 25,000 testing. ImageJ-processed segmentations (red = pores) used to compute area the pore fractions of Fig.3c. **a, b,** Yellow dashed lines indicate the marked area used for local analysis. Low Magnification (1.5 K X)

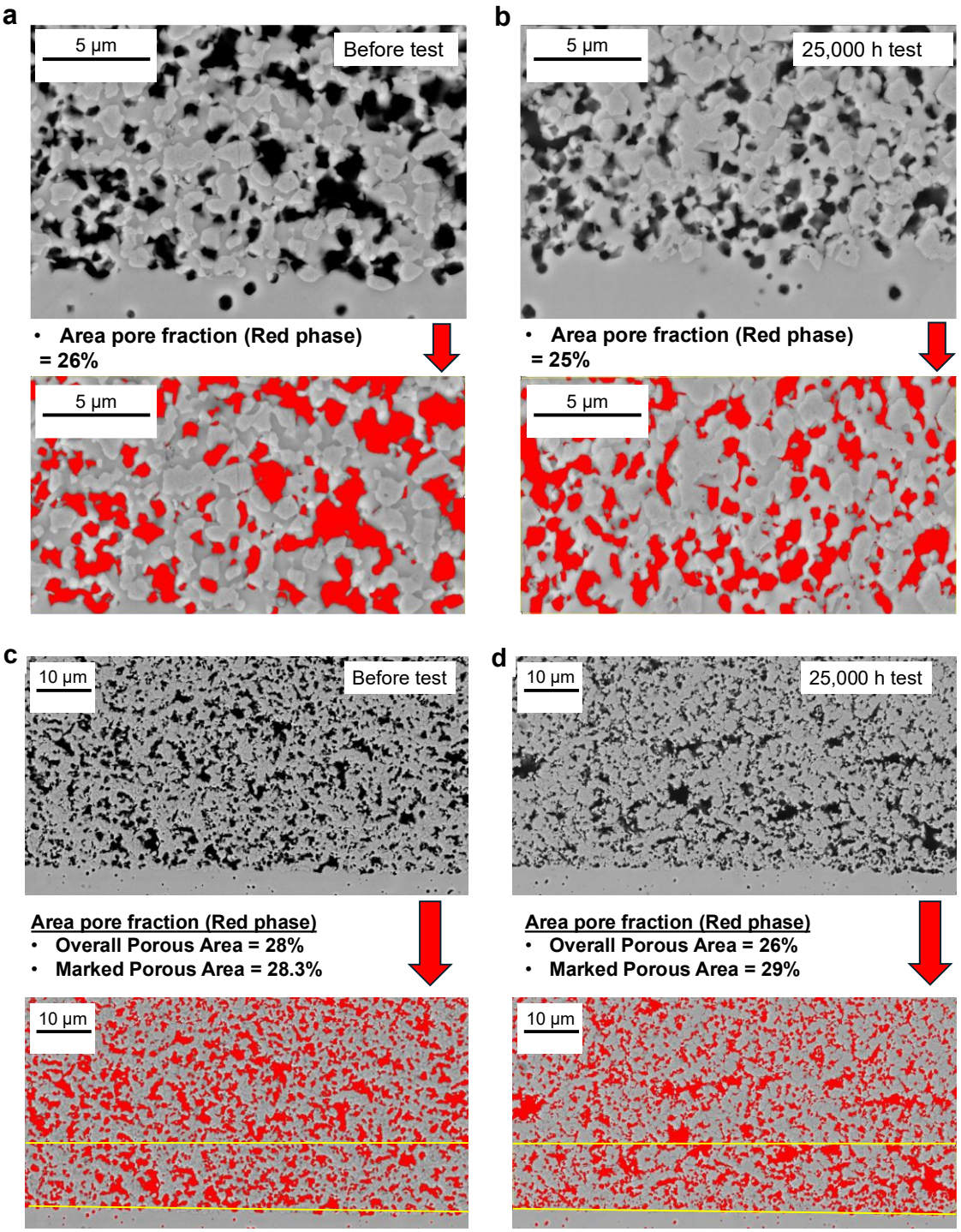

Fig. S8. Area pore-fraction analysis based on AsB-SEM images at the inlet of the Ni-YSZ FE before and after 25,000 testing. a, Images acquired before testing; and **b,** after 25,000 h of operation, both taken at high magnification (15 K X); **c**, Images acquired before testing; and **d**, after 25,000 h of operation, taken at low magnification (3.66 K X).The top panels show the raw AsB-SEM images, while the bottom panels present the corresponding ImageJ-processed segmentations (red = pores) used for area-fraction quantification. Yellow dashed lines indicate the regions used for local pore-fraction analysis.

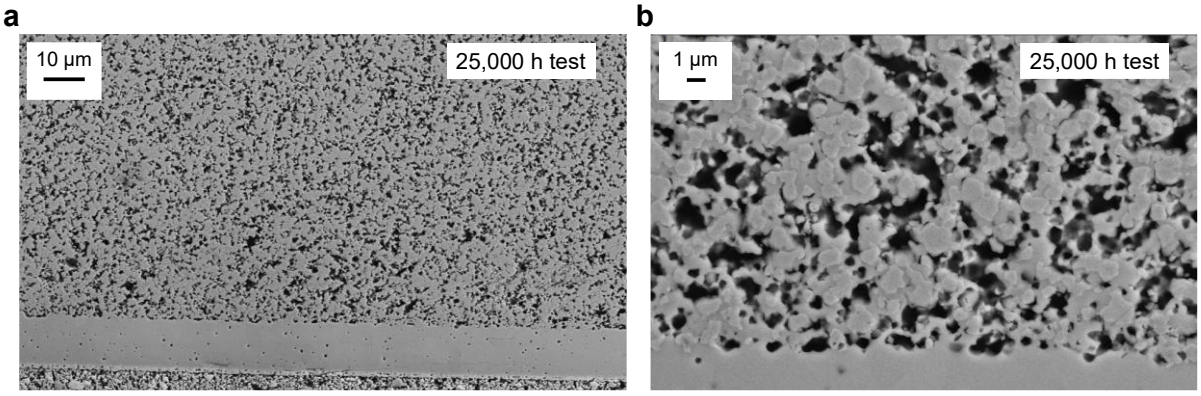

Fig. S9. AsB-SEM images at the outlet of the 25,000 h tested Ni–YSZ FE. a, Low magnification image (3.66 K X); **b,** Corresponding high magnification image (15 K X). Porosity is rendered in black and solid phases in grey; the YSZ electrolyte appears as the dense band at the bottom of each panel. No interfacial damage (black rims) is detected.

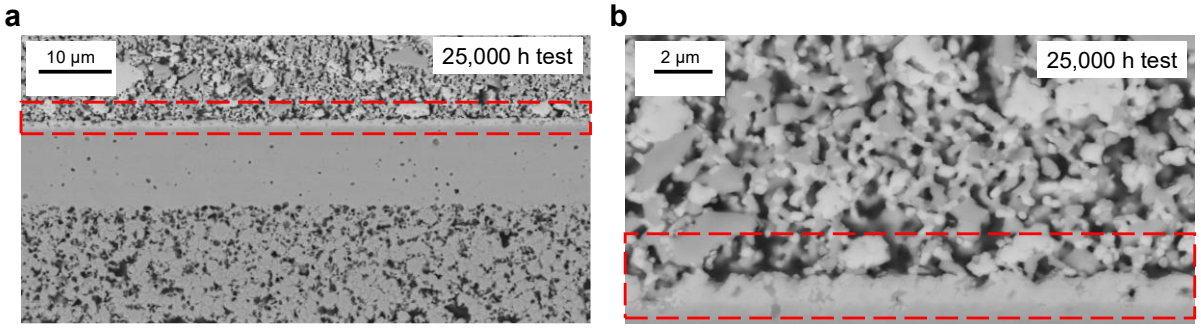

Fig. S10. AsB-SEM images at the inlet region of the 25,000 h tested SOEC. The interfaces between the YSZ electrolyte, the CGO barrier layer, and the LSCF–CGO OE OE are indicated at different magnifications. The porous region adjacent to this interface shows no evidence of infilling; the boundary is mechanically sharp and intact, with no visible secondary phase between the YSZ/CGO interface and the CGO/LSCF-CGO interface. Porosity is rendered in black and solid phases in grey; the YSZ electrolyte appears as the dense band at the bottom of each panel.

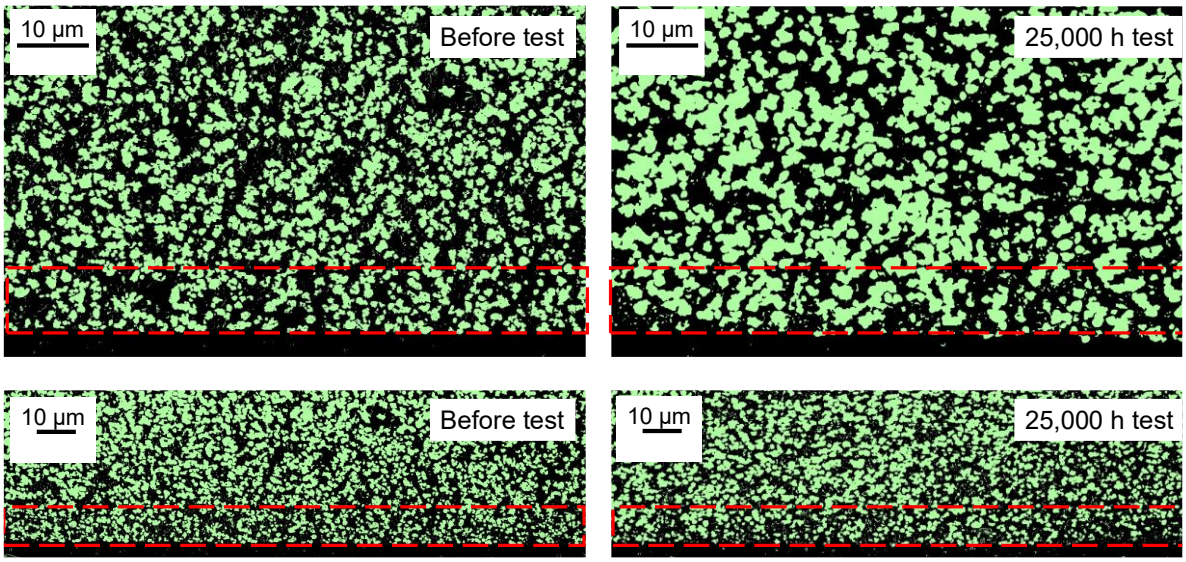

Fig. S11. Inlens-SEM images at the inlet of Ni–YSZ FE before testing and after 25,000 h. (Left column) Cross-sectional images of the Ni–YSZ fuel electrode prior to testing, acquired at two magnifications. (Right column) Corresponding BSE images after ~25,000 h of AC:DC operation, acquired at matched magnifications. The green overlay marks the percolated Ni network, which remains continuous from the bulk of the electrode to the YSZ electrolyte interface (dark band at the bottom of each panel), indicating that electronic percolation is preserved after AC:DC long-term operation.

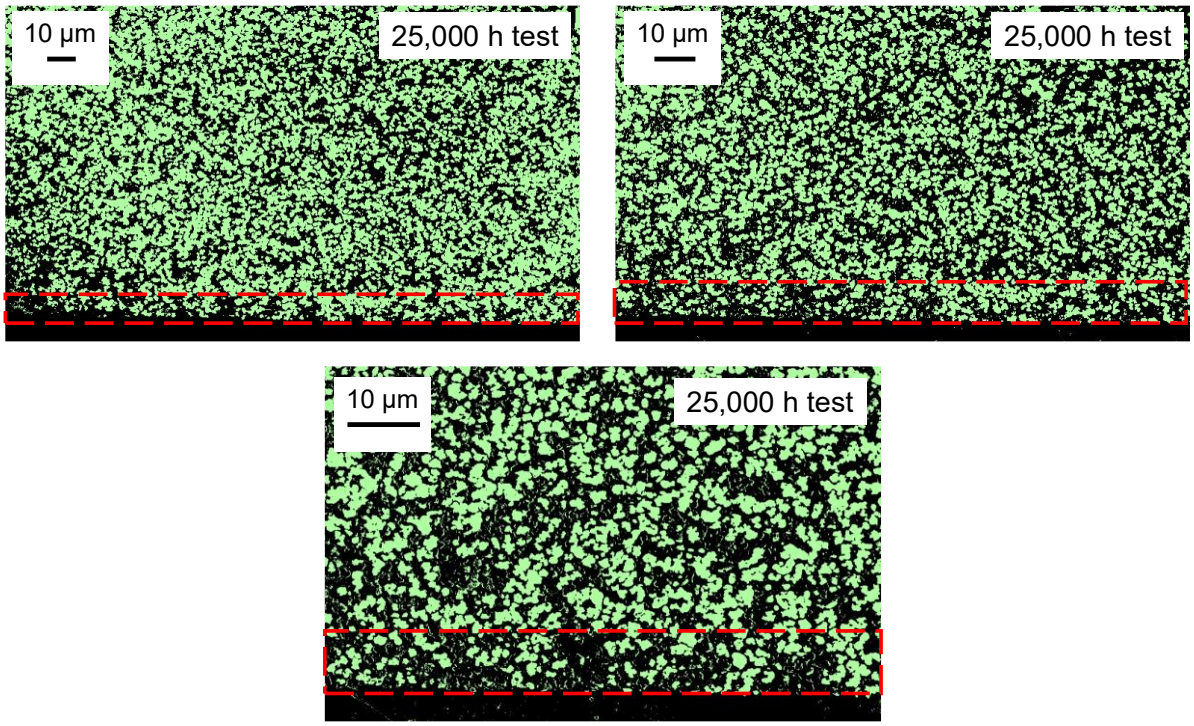

Fig. S12. Inlens-SEM images at the outlet of the 25,000 h tested Ni–YSZ FE. Cross-sectional images of the Ni–YSZ FE after ~25,000 h of AC:DC operation, acquired at three magnifications and different neighbouring locations. The green overlay marks the percolated Ni network, which remains continuous from the bulk of the electrode to the YSZ electrolyte interface (dark band at the bottom of each panel), indicating that electronic percolation is preserved after AC:DC long-term operation.

Supplementary Note.8. Energy Dispersive Xray Spectroscopy (EDS).

Elemental analysis was performed using the same SEM platform equipped with a Bruker Quantax Xray detector. A working distance of 8.5 mm and accelerating voltage of 15 kV was used for all EDS measurements, corresponding to an electron interaction volume of approximately 600 nm^3 [33]. EDS was employed for two purposes: (i) to map the elemental composition across the Ni–YSZ FE and LSCF-CGO OE, and (ii) to detect Si, Al, S and Cr contamination within the FE and OE, as well as to identify Sr presence within the CGO barrier layer and the YSZ electrolyte.

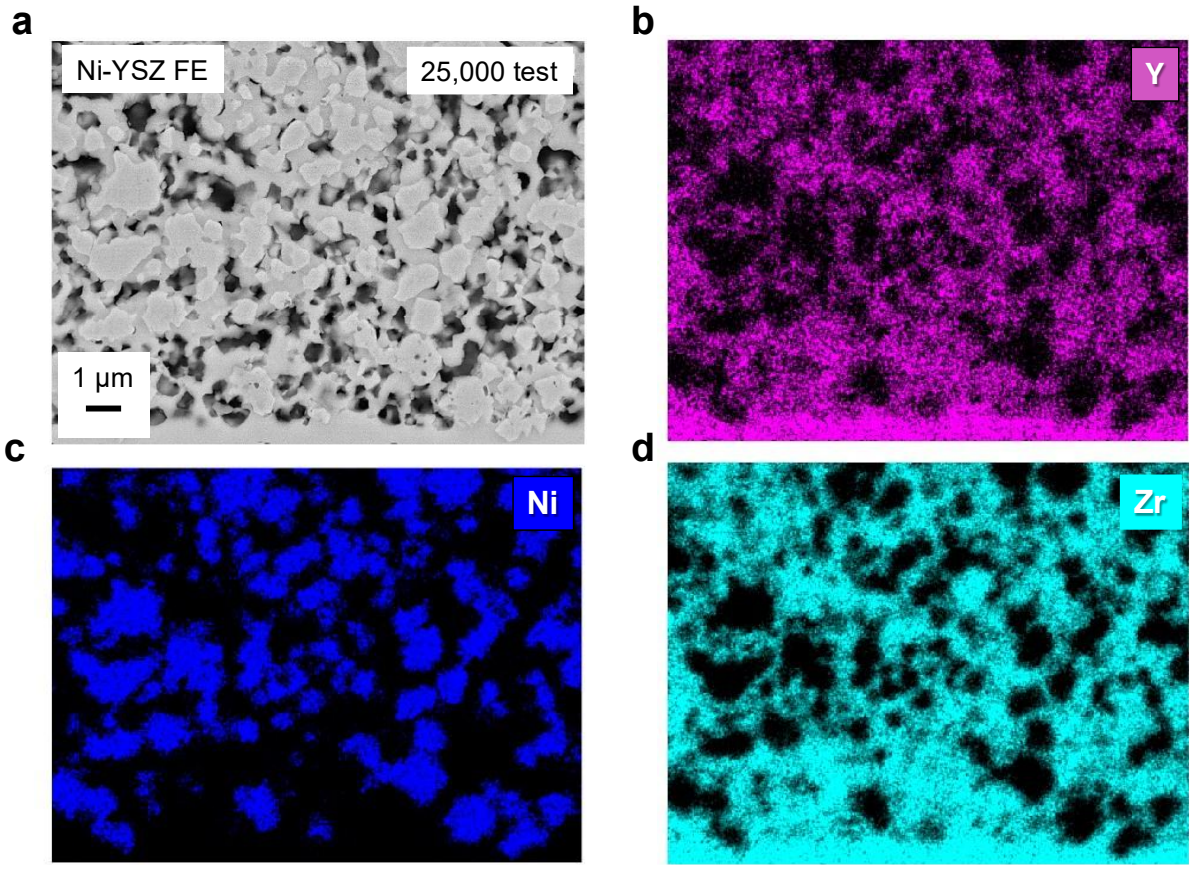

Fig. S13. Microstructure and elemental distribution of the 25,000 h tested Ni–YSZ FE. a, Cross-sectional AsB-SEM image of the porous Ni–YSZ fuel electrode after 25,000h of operation. Energy-dispersive X-ray spectroscopy (EDS) maps from the same field of view showing; **b,** Y (magenta), **c,** Ni (blue), and **d,** Zr (cyan). All elemental maps share the field of view in (a).

a

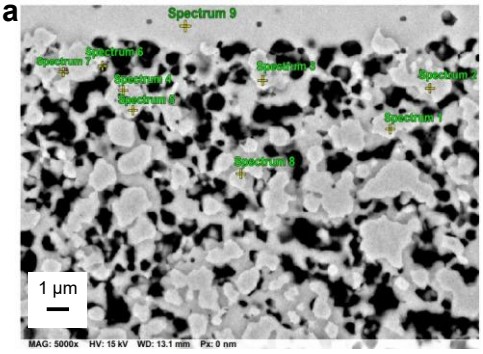

b

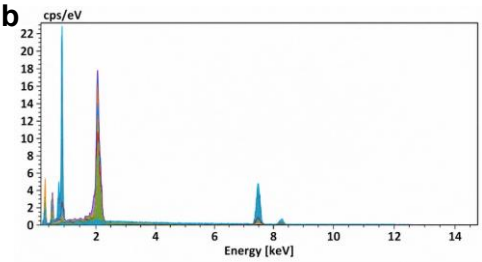

c

Element	Atom.(%)								
	Sp1	Sp2	Sp3	Sp4	Sp5	Sp6	Sp7	Sp8	Sp9
Al	0.25	4.73	0.68	0.07	0.56	0.06	0.04	0.68	0.32
Si	0.28	0.02	0.20	0.00	0.69	0.55	0.07	0.20	0.41
Cr	0.00	0.00	0.00	0.00	0.06	0.00	0.00	0.00	0.00
Ni	97.9	14.17	9.70	5.25	7.46	78.03	13.44	34.30	3.10
Y	0.12	4.86	5.85	6.05	6.79	1.45	5.73	4.75	12.84
Zr	1.45	76.25	83.56	88.63	84.45	19.91	80.72	59.99	83.32

Fig. S14. Cross-sectional microstructure and EDS point analysis of different black spots at the Ni-YSZ FE after tested for 25,000 h. a, Cross-sectional AsB-SEM image with EDS spot locations (Spectra 1–9) indicated. **b,** Summary of the EDS spectrum for all the spots. **c,** Quantified atomic concentrations (at.%) for Al, Si, Cr, Ni, Y, and Zr at each spot; mean and s.d. are summarized in the table taken directly from the software of the instrument. The impurity elements (Al, Si, and Cr) are present at trace levels (≤ ~1 at.%) and near the EDS detection limit.

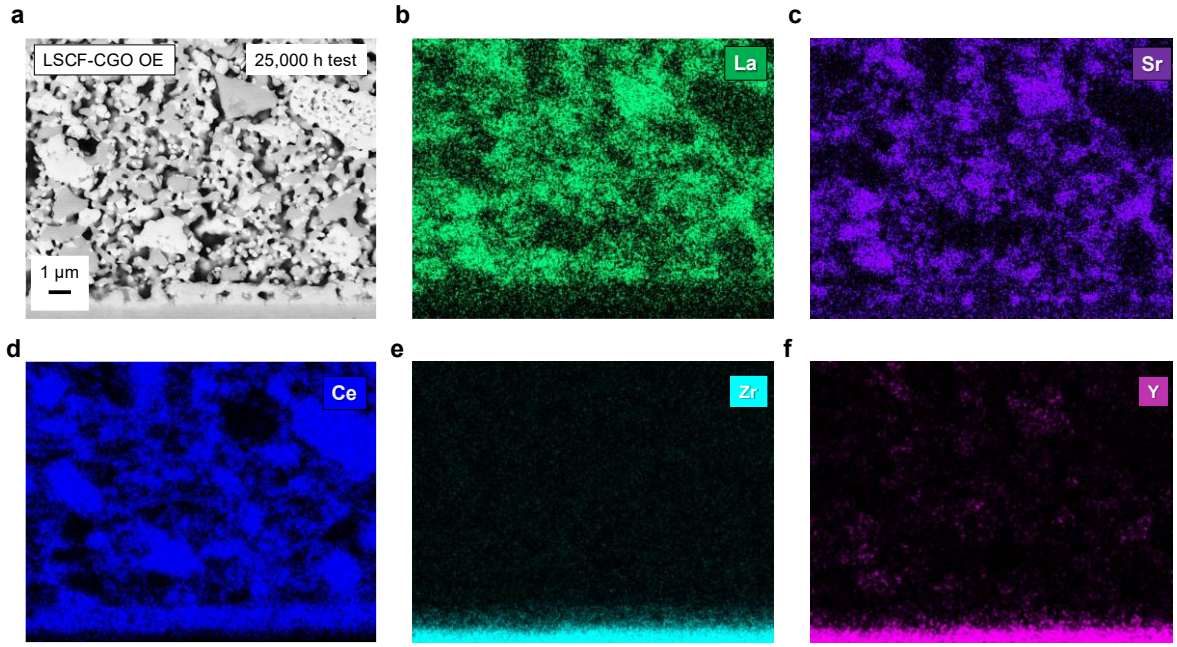

Fig. S15. Cross-sectional microstructure and elemental map analysis of the and Sr-rich regions in the LSCF-CGO OE and CGO barrier layer after the 25,000 h test. a, Cross-sectional AsB-SEM image of the porous LSCF–CGO oxygen electrode. Energy-dispersive X-ray spectroscopy (EDS) maps from the same field of view showing; **b,** La (green); **c,** Sr (purple); **d,** Ce (blue); **e,** Zr (cyan); **f,** (magenta), ; **g,** Si (green); **h,** Al (red), and **j,** Cr (yellow). La and Sr are co-localized, consistent with the LSCF phase, whereas Ce highlights also the CGO barrier layer. Zr and Y are confined to a narrow band at the bottom of the field of view, consistent with the underlying YSZ electrolyte. No Sr is detected within the CGO barrier layer and the YSZ electrolyte; apparent colour within the pores of the CGO layer arises from the background. For Si, Al, and Cr, the measured counts are at or below the EDS detection limit; the high-gain display produces a uniform speckled appearance that can be misread as widespread signal. These impurity maps should therefore be interpreted as below-detection rather than evidence of pervasive contamination. All elemental maps are co-registered to (a).

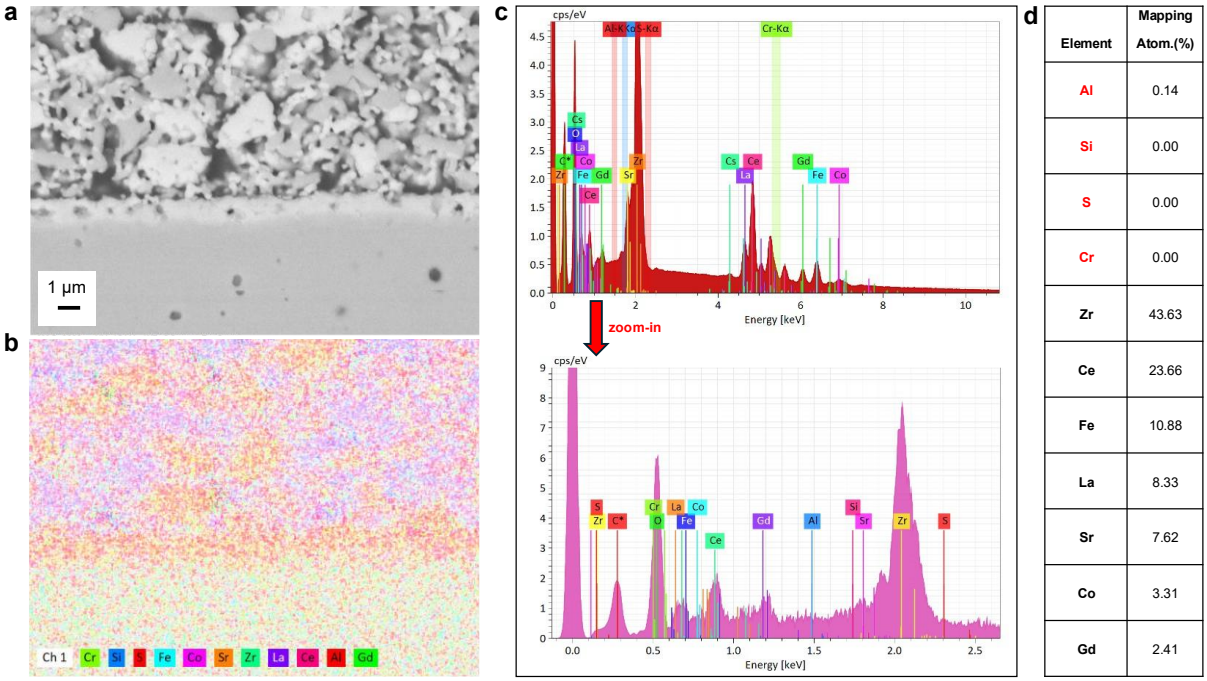

Element	Mapping Atom.(%)
Al	0.14
Si	0.00
S	0.00
Cr	0.00
Zr	43.63
Ce	23.66
Fe	10.88
La	8.33
Sr	7.62
Co	3.31
Gd	2.41

Fig. S16. Cross-sectional microstructure and elemental analysis of the LSCF-CGO/CGO10/YSZ/Ni-YSZ half-cell after the 25,000 h test. a, Cross-sectional AsB-SEM image showing the porous oxygen electrode and dense electrolyte region. **b,** Corresponding EDS illustrative elemental map. **c,** Corresponding EDS spectra of the investigated cross-sectional image, indicating characteristic peaks of the constituent elements. **d,** Corresponding quantitative EDS elemental composition extracted from the mapped region. The red-highlighted elements (Al, Si, S and Cr), commonly observed impurities in SOFC materials, appear at levels below the detectable limit of the EDS measurement,

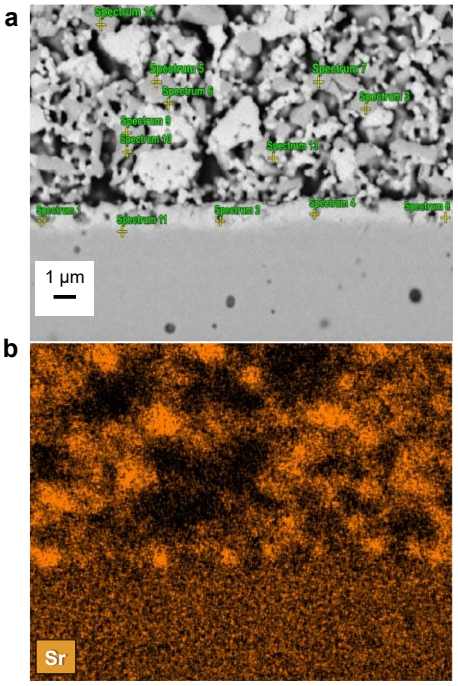

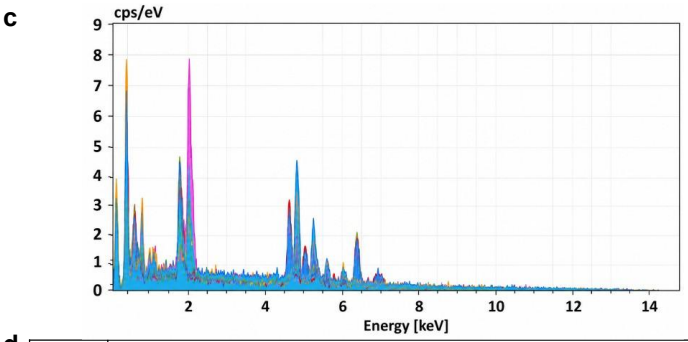

d

Element	Atom. (%)												
	Sp1	Sp2	Sp3	Sp4	Sp5	Sp6	Sp7	Sp8	Sp9	Sp10	Sp11	Sp12	Sp13
Al	0.76	0.78	0.05	1.73	1.12	0.58	0.82	0.34	0.18	0.30	0.78	0.00	0.00
Si	1.13	0.78	0.63	1.51	0.99	0.59	0.04	0.06	0.25	0.22	0.44	0.00	0.27
S	0.76	0.78	0.05	0.03	0.73	0.58	0.00	0.00	0.00	0.26	0.00	0.00	0.00
Cr	0.76	1.07	0.05	0.48	0.74	0.59	0.00	0.00	0.00	0.00	0.25	0.00	0.00
Fe	1.24	2.95	0.43	0.83	37.79	38.17	36.98	38.99	30.29	38.54	0.10	43.19	34.02
Co	1.09	1.44	0.43	0.70	10.10	11.90	9.02	9.77	9.21	8.37	4.87	7.92	8.68
Sr	16.17	15.65	10.79	6.79	15.13	19.21	22.56	19.91	14.86	21.84	3.03	21.28	18.40
Zr	16.17	22.74	17.43	14.94	0.91	0.59	0.09	0.00	0.00	0.16	46.9	0.00	0.00
La	2.55	2.75	2.33	2.09	25.10	23.83	24.54	27.90	21.89	28.55	0.22	25.56	22.29
Ce	53.38	45.93	62.51	63.9	5.97	2.62	5.32	3.01	19.56	1.92	38.4	3.41	14.86
Gd	5.99	5.13	5.30	6.30	1.42	1.34	0.77	0.06	3.79	0.00	4.95	0.00	1.48

Fig. S17. Cross-sectional microstructure and elemental analysis of the and Sr-rich regions in the LSCF-CGO OE and CGO barrier layer after the 25,000 h test. a, Cross-sectional AsB-SEM image showing the porous electrode and dense electrolyte region, with EDS sampling points placed within the CGO barrier layer and in the Sr-rich secondary phase of the OE. **b,** EDS elemental map of Sr highlighting the distribution of Sr-enriched regions within the OE microstructure. **c,** Summary of the EDS spectra collected from all sampling locations. **d,** Quantitative atomic composition from 13 points. The red-highlighted elements (Al, Si, S and Cr), which are common impurities and are known to nucleate preferentially on Sr-rich phases, appear at levels below the detectable limit in both the CGO layer and the Sr-containing electrode regions, confirming the absence of measurable Sr-driven contamination.

Table S6. Summary of economic assumptions and SOEC stack operation conditions for the base case scenario.

Parameter	Value
System size	~ 1 GW
Hot module size	1 MW
Capacity factor	50 %
SOEL stack cost	(685 + 30% markup) € m^{-2}
Levelized cost of electricity	50 €/MWh
Available free steam	100 %
Interest rate	8 %
Maximum allowed temperature at the cold module	675 °C
Minimum temperature difference of the HEXs (size of HEXs)	200 °C
Maximum pressure drop in heat exchangers	0.1 bar
Efficiency of electrical heaters	98 % [34]
Efficiency of rectifier	98 % [35]
Efficiency of compressors	80 % [36]
Efficiency of pump	75 % [37]
Current density	- 0.5 A cm^{-2}
Stack inlet temperature	750 °C
Stack oxygen to steam molar ratio (OS) at the inlet	0.2
Stack feedstock inlet composition (molar basis)	10% H_2 + 90% H_2O
Stack feedstock utilization	70%
Stack inlet air composition (molar basis)	21% O_2 + 79% N_2
Stack inlet pressure	1 bar
Stack pressure drop	2% of inlet pressure
Hot standby power consumption	5.5% of the total power demand

Supplementary Information references:

1. Santos, D. M. F., Sequeira, C. A. C. & Figueiredo, J. L. Hydrogen production by alkaline water electrolysis. Quim. Nova 36, 1176–1193 (2013). https://doi.org/10.1590/S0100-40422013000800017
2. Schmidt, O. et al. Future cost and performance of water electrolysis: an expert elicitation study. Int. J. Hydrogen Energy 42, 30470–30492 (2017). https://doi.org/10.1016/j.ijhydene.2017.10.045
3. International Renewable Energy Agency. Green Hydrogen Cost Reduction: Scaling Up Electrolysers to Meet the 1.5 °C Climate Goal (IRENA, 2020).
4. Shiva Kumar, S. & Lim, H. An overview of water electrolysis technologies for green hydrogen production. Energy Rep. 8, 13793–13813 (2022). https://doi.org/10.1016/j.egyr.2022.10.127
5. Shiva Kumar, S. & Himabindu, V. Hydrogen production by PEM water electrolysis – a review. Mater. Sci. Energy Technol. 2, 442–454 (2019). https://doi.org/10.1016/j.mset.2019.03.002
6. Weiß, A. et al. Impact of intermittent operation on lifetime and performance of a PEM water electrolyzer. J. Electrochem. Soc. 166, F487–F497 (2019). https://doi.org/10.1149/2.0421908jes
7. Felgenhauer, M. & Hamacher, T. State-of-the-art of commercial electrolyzers and on-site hydrogen generation for logistic vehicles in South Carolina. Int. J. Hydrogen Energy 40, 2084–2090 (2015). https://doi.org/10.1016/j.ijhydene.2014.12.043
8. Buttler, A. & Spliethoff, H. Current status of water electrolysis for energy storage, grid balancing and sector coupling via power-to-gas and power-to-liquids: a review. Renew. Sustain. Energy Rev. 82, 2440–2454 (2018). https://doi.org/10.1016/j.rser.2017.09.003
9. Anderson, E. PEM electrolyzer reliability based on 20 years of product experience in commercial markets. In 2nd International Workshop on Durability and Degradation Issues in PEM Electrolysis Cells and Its Components (2016).
10. Lewinski, K. A., van der Vliet, D. & Luopa, S. M. NSTF advances for PEM electrolysis – the effect of alloying on activity of NSTF electrolyzer catalysts and performance of NSTF-based PEM electrolyzers. ECS Trans. 69, 893–917 (2015). https://doi.org/10.1149/06917.0893ecst
11. Khan, M. A. et al. Recent progresses in electrocatalysts for water electrolysis. Electrochem. Energy Rev. 1, 483–530 (2018). https://doi.org/10.1007/s41918-018-0014-z

12. Hauch, A. et al. Recent advances in solid oxide cell technology for electrolysis. Science 370, eaba6118 (2020). https://doi.org/10.1126/science.aba6118
13. Hauch, A., Ploner, A., Pylypko, S., Cubizolles, G. & Mougin, J. Test and characterization of reversible solid oxide cells and stacks for innovative renewable energy storage. Fuel Cells 21, 467–476 (2021). https://doi.org/10.1002/fuce.202100046
14. Küngas, R. et al. Progress in SOEC development activities at Haldor Topsøe. ECS Trans. 91, 215–223 (2019). https://doi.org/10.1149/09101.0215ecst
15. Aicart, J. et al. Lifespan evaluation of two 30-cell electrolyte-supported stacks for hydrogen production by high temperature electrolysis. Int. J. Hydrogen Energy 60, 531–539 (2024). https://doi.org/10.1016/j.ijhydene.2024.02.239
16. Kindelmann, M., Guillon, O., Mayer, J. & Menzler, N. H. Atomic-scale insights into air electrode degradation after 10 years of fuel cell stack operation. J. Mater. Chem. A (2025). https://doi.org/10.1039/D5TA03917G
17. Blum, L. et al. Forschungszentrum Jülich – progress in SOC development. ECS Trans. 91, 2443–2453 (2019). https://doi.org/10.1149/09101.2443ecst
18. Liu, H., Yu, M., Tong, X., Wang, Q. & Chen, M. High temperature solid oxide electrolysis for green hydrogen production. Chem. Rev. 124, 10509–10576 (2024). https://doi.org/10.1021/acs.chemrev.3c00795
19. Fang, Q., Frey, C. E., Menzler, N. H. & Blum, L. Electrochemical performance and preliminary post-mortem analysis of a solid oxide cell stack with 20,000 h of operation. J. Electrochem. Soc. 165, F38–F45 (2018). https://doi.org/10.1149/2.0541802jes
20. Frey, C. E., Fang, Q., Sebold, D., Blum, L. & Menzler, N. H. A detailed post mortem analysis of solid oxide electrolyzer cells after long-term stack operation. J. Electrochem. Soc. 165, F357–F364 (2018). https://doi.org/10.1149/2.0961805jes
21. Rinaldi, G. et al. Post-test analysis on a solid oxide cell stack operated for 10,700 hours in steam electrolysis mode. Fuel Cells 17, 541–549 (2017). https://doi.org/10.1002/fuce.201600194
22. Corre, G. & Brisse, A. 9000 hours operation of a 25 solid oxide cells stack in steam electrolysis mode. ECS Trans. 68, 3481–3490 (2015). https://doi.org/10.1149/06801.3481ecst
23. Megel, S. et al. Co-electrolysis with CFY-stacks. ECS Trans. 78, 3089–3102 (2017). https://doi.org/10.1149/07801.3089ecst
24. Chen, M. & Brodersen, K. Solid oxide electrolysis for grid balancing. ResearchGate preprint. https://doi.org/10.13140/RG.2.2.20291.09760

25. Léon, A., Micero, A., Ludwig, B. & Brisse, A. Effect of scaling-up on the performance and degradation of long-term operated electrolyte-supported solid oxide cell, stack and module in electrolysis mode. J. Power Sources 510, 230346 (2021). https://doi.org/10.1016/j.jpowsour.2021.230346
26. Lang, M., Raab, S., Lemcke, M. S., Bohn, C. & Pysik, M. Long-term behavior of a solid oxide electrolyzer (SOEC) stack. Fuel Cells 20, 690–700 (2020). https://doi.org/10.1002/fuce.201900245
27. Hjalmarsson, P. et al. Current status of Ceres electrolysis programme. ECS Trans. 111, 977–989 (2023). https://doi.org/10.1149/11106.0977ecst
28. Skafte, T. L. et al. Electrothermally balanced operation of solid oxide electrolysis cells. J. Power Sources 523, 231040 (2022). https://doi.org/10.1016/j.jpowsour.2022.231040
29. Mattera, F., Smitshuysen, T. E. L., Liso, V. & Jensen, S. H. Experimental syngas production via co-electrolysis with AC:DC operated solid oxide cells for downstream fuel synthesis. J. Power Sources 647, 239904 (2026). https://doi.org/10.1016/j.jpowsour.2026.239904
30. Yrjänä, V. DearEIS – a GUI program for analyzing impedance spectra. J. Open Source Softw. 7, 4808 (2022). https://doi.org/10.21105/joss.04808
31. Knibbe, R. Microstructural degradation of Ni–YSZ anodes for solid oxide fuel cells. PhD thesis, Technical University of Denmark (2010).
32. Schneider, C. A., Rasband, W. S. & Eliceiri, K. W. NIH Image to ImageJ: 25 years of image analysis. Nat. Methods 9, 671–675 (2012). https://doi.org/10.1038/nmeth.2089
33. Trini, M. et al. Comparison of microstructural evolution of fuel electrodes in solid oxide fuel cells and electrolysis cells. J. Power Sources 450, 227599 (2020). https://doi.org/10.1016/j.jpowsour.2019.227599
34. AlZahrani, A. A. & Dincer, I. Modeling and performance optimization of a solid oxide electrolysis system for hydrogen production. Appl. Energy 225, 471–485 (2018). https://doi.org/10.1016/j.apenergy.2018.04.124
35. Reznicek, E. P. & Braun, R. J. Reversible solid oxide cell systems for integration with natural gas pipeline and carbon capture infrastructure for grid energy management. Appl. Energy 259, 114118 (2020). https://doi.org/10.1016/j.apenergy.2019.114118
36. Cai, D. et al. Cost and thermodynamic analysis of wind-hydrogen production via multi-energy systems. Energy Convers. Manag. 306, 118286 (2024). https://doi.org/10.1016/j.enconman.2024.118286
37. Hara, N., Taniguchi, S., Yamaki, T., Nguyen, T. T. H. & Kataoka, S. Impacts of hydrogen price and carbon dioxide emission factor on bi-objective optimizations of absorption and

subsequent methanation processes of carbon dioxide capture, utilization, and storage. J. Clean. Prod. 456, 142358 (2024). https://doi.org/10.1016/j.jclepro.2024.142358